Cerebral Cortex October 2008;18:2318–2330
doi:10.1093/cercor/bhm259
Advance Access publication January 24, 2008

The Microvascular System of the Striate and Extrastriate Visual Cortex of the Macaque

Bruno Weber[1,2], Anna Lena Keller[1], Johannes Reichold[3] and Nikos K. Logothetis[1]

[1]Max-Planck Institut für biologische Kybernetik, Spemannstr. 38, 72076 Tübingen, Germany, [2]University of Zurich, Institute for Pharmacology and Toxicology, Rämistrasse 100, 8091 Zurich, Switzerland and [3]Swiss Federal Institute of Technology, Institute for Fluid Dynamics, Sonneggstrasse 3, 8092 Zurich, Switzerland

In functional neuroimaging, neurovascular coupling is used to generate maps of hemodynamic changes that are assumed to be surrogates of regional neural activation. The aim of this study was to characterize the microvascular system of the primate cortex as a basis for understanding the constraints imposed on a region's hemodynamic response by the vascular architecture, density, as well as area- and layer-specific variations. In the macaque visual cortex, an array of anatomical techniques has been applied, including corrosion casts, immunohistochemistry, and cytochrome oxidase (COX) staining. Detailed measurements of regional vascular length density, volume fraction, and surface density revealed a similar vascularization in different visual areas. Whereas the lower cortical layers showed a positive correlation between the vascular and cell density, this relationship was very weak in the upper layers. Synapse density values taken from the literature also displayed a very moderate correlation with the vascular density. However, the vascular density was strongly correlated with the steady-state metabolic demand as measured by COX activity. This observation suggests that although the number of neurons and synapses determines an upper bound on an area's integrative capacity, its vascularization reflects the neural activity of those subpopulations that represent a "default" mode of brain steady state.

Keywords: capillaries, cerebral blood flow, collagen, monkey, neuroimaging, primate

Introduction

Despite its relatively small size the brain consumes roughly a quarter of the body's total glucose and a fifth of the oxygen. The high energy demand in combination with the fact that brain tissues lack any substantial capacity to store energy requires a tight spatiotemporal control of the energy supply. Changes in neural activity are indeed followed by precisely controlled changes in hemodynamics, as hypothesized more than a century ago (Mosso 1881; Roy and Sherrington 1890). This remarkable site- and time-specific neurovascular coupling has been systematically exploited to generate detailed maps of hemodynamic changes that are assumed to be surrogates of the actual regional neural activation. A recent celebrated example is the so-called blood oxygenation level–dependent (BOLD) contrast (Ogawa et al. 1990; Kwong et al. 1992) of magnetic resonance imaging (MRI), which reflects a complicated interplay of changes in blood volume, blood flow, and oxygen consumption (Logothetis and Wandell 2004). Because BOLD functional MRI (fMRI) is now the mainstay of biomedical neuroimaging, a lot of research has been focused recently on the functional aspects of neurovascular coupling, including the underlying signaling mechanisms, and the biochemistry of the neurometabolic link. Yet understanding neurometabolic and neurovascular coupling also requires a comprehension of the significant constraints imposed by architecture, density, and area-specific variation in the vascular system.

In response to this, a great deal of research is currently being devoted to understanding and modeling the link between neural activation and BOLD or perfusion fMRI (Logothetis et al. 2001; Devor et al. 2003; Jones et al. 2004; Sheth, Nemoto, Guiou, Walker, Pouratian, Toga, 2004; Thomsen et al. 2004; Martindale et al. 2005) or to describing the spatiotemporal dynamics of the hemodynamic response (Sheth, Nemoto, Guiou, Walker, Pouratian, Hageman, et al. 2004; Vanzetta et al. 2004; Weber et al. 2004; Sheth et al. 2005).

Ultimately, the spatial resolution and specificity of the hemodynamic response maps rely not only on the cascade of neurovascular signaling, but also on the vascular architecture and spatial level of blood flow regulation. Little is known, however, about the principles of flow regulation at different vascular scales, about the spatial distribution of vascular densities, and about the dependence of vasculature on cortical areas or brain sites in general. In their seminal study, Duvernoy et al. (1981) demonstrated area-specific vascular densities in the human brain, but unfortunately failed to provide precise quantitative data.

More recently, it was shown that areas with higher steady-state metabolic demand show a higher degree of vascular density (Zheng et al. 1991; Cox et al. 1993; Riddle et al. 1993; Woolsey et al. 1996; Tieman et al. 2004). In a study employing the corrosion cast technique together with optical imaging, Harrison et al. (2002) postulated a close relationship between the hemodynamic response map and both vascular density and the localization of perivascular flow control elements. All of these studies quantified the vasculature within a primary sensory area, or at best compared it with a secondary region. Investigations of a more complete hierarchical system—such as large parts of the visual system—have yet to be carried out. Because fMRI has the great advantage of measuring brain activity with full coverage, countless studies have compared the activity in different cortical areas. However, the completely different vascular densities and architectures of these regions would impede direct comparisons of the local readouts based on the hemodynamic response.

In this work, we describe and quantify the microvasculature in the macaque visual cortex, applying 2 different and complementary techniques. Scanning electron microscopy was used to image vascular corrosion casts for a qualitative assessment of the microvascular organization, for an estimation of the ratio between arteries and veins, as well as for an investigation of perivascular structures. At the same time,

double histochemical stains were performed on a large data set from 3 monkeys to evaluate quantitative layer- and area-specific vascular densities. To compare the vascular density with the basal metabolic demand of a given region, cytochrome oxidase (COX) stains were prepared in 3 additional subjects.

Materials and Methods

Animals

The brains of 7 adult monkeys (*Macaca mulatta*) were used in this study. The animals were involved in chronic combined physiological and behavioral experiments. At the end of the experiments and as part of our standard protocol the animals were killed with an overdose of pentobarbital (120 mg/kg). The euthanasia methods correspond to the guidelines of the "American Veterinary Association Panel on Euthanasia" and to the recommendations of the "Guide for the Care and Use of Laboratory Animals of the National Institutes of Health of the United States." They were all approved by the local authorities (Regierungspräsidium) and are also in full compliance with the guidelines of the European community (EUVD 86/609/EEC) for the care and use of laboratory animals. The brain of one of the animals was used for vascular corrosion casts, 3 brains were used for histochemical processing and 3 were stained for COX activity.

Vascular Corrosion Casts

The animal was perfused under deep sodium pentobarbital (120 mg/kg) anesthesia with 0.9% warm heparinized 0.1 M phosphate buffered saline (PBS) through a catheter in the ascending aorta. Then, Batson's #17 resin (Polysciences Inc., Eppelheim, Germany) was injected. After full polymerization overnight, the brain was carefully removed from the skull. The monkey brains were frozen at –20 °C and cut in cubes of about 15 × 15 × 15 mm using a dedicated saw. Brain tissue cubes were macerated in 5% KOH. The maceration process, which included daily rinses in water, took about 1 week. The polymer filling was then frozen in distilled water and the regions of interest were trimmed using a cryostat, yielding precise cuts without any damage of the fragile cast (see Figs 1 and 2). The specimens were then lyophilized overnight and sputter coated with gold. Scanning electron microscopy at 10–20 kV (Hitachi S-800) was then used to acquire high-resolution images of the vascular corrosion casts. Large vessels penetrating the cortex from the surface were individually imaged. On these high magnification images, each vessel could be identified as either an artery or a vein on the basis of the form of the imprints of the endothelial cell nuclei (Miodonski et al. 1976). As described before, arteries show shallow and elliptical or lens-shaped imprints. In contrast, the endothelial cell nuclei imprints on the venous lumen are more circular and the vessels have a more sluggish appearance due to the lower blood pressure in the venous system. In total, we analyzed 249 vessels that could be identified with sufficient certainty, from which we could estimate the ratio between arteries and veins. The shrinkage of the employed resin is known to be small (Lametschwandtner et al. 1990) and was disregarded in this study.

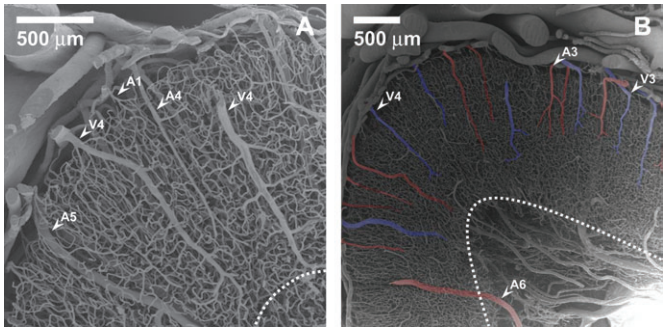

Figure 1. Scanning electron micrographs of a vascular corrosion cast from monkey visual cortex (superior temporal gyrus). Casts were cut and trimmed to allow a vertical view on the cortex. The gray–white matter demarcation line is shown as dashed line. Note the continuous orderly distribution of large vessels oriented perpendicularly to the cortical surface, their different length and branching patterns and the rather homogeneous mesh size and density of the capillary bed. The arrowheads in (*A*) and (*B*) exemplify a few vessel types, named according to the different vessel classes introduced by Duvernoy et al. (1981) for the human brain. According to this classification, a vessel of class 1 would for example feed/drain the capillary bed in the vascular layer 1, whereas a class 6 artery would traverse the cortex without any branching in gray matter. In Figure 1*B*, the larger penetrating arteries are shaded red and the veins are shaded blue. (A = artery, V = vein, 1–6 = category based on their cortical depth; scale bars = 500 µm.)

Histochemistry

Three animals were perfused transcardially under deep sodium pentobarbital (120 mg/kg) anesthesia with 8 L of warm heparinized 0.1 M PBS, followed by 2 L of cold 1% paraformaldehyde (PFA) in 0.1 M phosphate buffer (PB), then 4 L of 4% PFA in 0.1 M PB, and finally 1–2 L of 10% sucrose in 0.1 M PB. The brain was removed from the skull and stored in 4% PFA at 4 °C. Before sectioning, cortical blocks were placed in ascending concentrations of sucrose in 0.1 M PB (10%, 20%, and 30%) until they sank. Sixty-micrometer-thick horizontal frozen sections were then cut serially on a sliding microtome (Microm HM 440E, Walldorf, Germany) and stored at –20 °C in cryoprotectant (30% ethylene glycol and 10% sucrose in 0.05 M PB) until further processing. Double fluorescence histochemical staining was carried out on every tenth free-floating section. Sections were rinsed 3 times for 5 min each in 0.1 M PBS before and after antigen retrieval (incubation overnight in 0.05 M TRIS buffer at 65 °C). They were then blocked with TRIS saline pH 7.4 (0.6% TRIS) containing 0.02% sodium azide, 5% dry milk, 1% Triton X-100 (Sigma, Schnelldorf, Germany), and 1% goat serum for 1 h at room temperature. Anticollagen has been successfully used to stain all types of cerebral vessels (arteries, capillaries, and veins) with excellent specificity (Hamann et al. 1995; Fukuda et al. 2004). The primary antibody (monoclonal anticollagen type IV, clone col-94; Sigma) was diluted 1:500 in TRIS saline containing 2% bovine serum albumin (albumin bovine fraction V powder, Sigma), 0.05% thimerosal (Sigma), and 1% Triton X-100 and the sections were incubated in this solution overnight at 4° C. They were then washed again 3 times in 0.1 M PBS before being incubated overnight at 4 °C in the dark in a solution containing the secondary antibody (Cy-3–conjugated goat anti-mouse IgG (H + L), Jackson ImmunoResearch, West Grove, PA, diluted 1:500 in PBS containing 1% goat serum). In between 2 series of 3 rinses in 0.1 M PBS the sections were incubated for 5 min in 0.4 × 10^{-3}‰ DAPI (4′,6-diamidino-2-phenylindole dihydrochloride; Sigma) in dH_2O. Stained sections were mounted on glass slides and cover-slipped with polyvinyl alcohol (Mowiol 4-88; Hoechst, Frankfurt, Germany) containing 4% 1,4-diazobicyclooctane (Merck, Darmstadt, Germany) as an antifading reagent. Consecutive sections were stained for Nissl and myelin (Werner'sche Markscheidenfärbung). The tissue shrinkage due to the perfusion and fixation was assumed to be minimal. The shrinkage produced by subsequent tissue handling was measured according to the protocol described in O'Kusky and Colonnier (1982), and was found to be 5%. It is important to note that this value is rather small due to the fact that the sections were not dry-mounted.

Fluorescence Microscopy

Cy-3 and DAPI images of identical fields of view were acquired using a fluorescence microscope (Axiophot, 5× objective; Carl Zeiss, Göttingen, Germany) equipped with a CCD camera (Axiocam MRm, controlled by Axiovision 4.3; Zeiss, Göttingen, Germany).

Data Analysis

Measurements were made on images extending from cortical layer I to white matter (approximately 1 × 2 mm in size). The specific cortical visual areas were identified with the help of an anatomic atlas (Saleem and Logothetis 2006). Within a visual area, images were taken from locations without obvious histological damage. All digital image processing was performed using Matlab (Mathworks, Natick, MA). The raw anticollagen images (Fig. 3*C,E*) were median filtered and thresholded to yield binary images of the vessels (Fig. 3*D,F*). The total projected vessel length was computed on the eroded traces (Fig. 3*G*). The volume fraction (%), length density (mm/mm^3), surface density (mm^2/

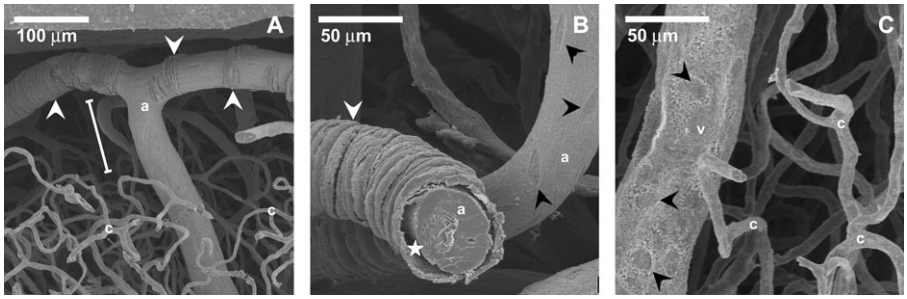

Figure 2. Details of coronal view on a vascular corrosion cast from monkey visual cortex. (*A*) Superficial artery with perivascular elements, so-called plastic strips. The white bar marks the upper molecular layer which is devoid of capillaries. (*B*) Plastic strip surrounding artery. Note the gap between the vessel lumen and the plastic strip (asterisk). Alongside this vessel runs another artery without plastic strips, showing the typical elongated imprints of arterial endothelial cell nuclei. (*C*) Vein with circular imprints of endothelial cell nuclei, in contrast to the longish arterial ones. (White arrowheads = plastic strips; black arrowheads = imprints of endothelial nuclei, a = artery, v = vein, c = capillary.)

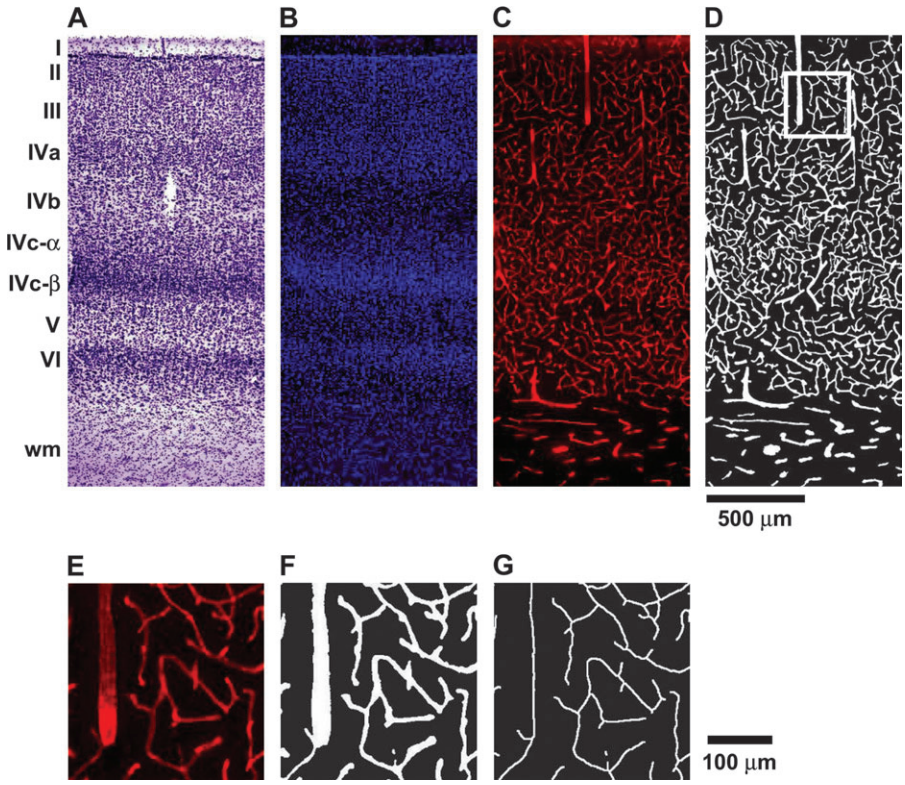

Figure 3. Double fluorescence stainings of the macaque visual area V1. (*A*) Nissl stain, with easily identifiable laminae of striate cortex (wm = white matter), consecutive section to (*B–G*); (*B*) DAPI stain used for identification of cortical laminae, note the good correspondence of cell nuclei density to Nissl stain; (*C*) raw image of a Cy-3 anticollagen type IV stain used for the quantification of the vessels (*B* and *C* identical sections); (*D*) Filtered and thresholded binary vessel image (same as *B*); (*E–G*) magnified subarea indicated in (*D*) to illustrate image quality; (*G*) eroded trace of binary vessel image.

mm^3), and mean vessel diameter (µm) were then computed stereologically (taking into account the bias induced by the finite section thickness; Russ and Dehoff 2000; see Appendix for details of the quantification assumptions and methods) for regions of interest (ROIs) representing the cortical layers. The density and diameter values were separately assessed for capillaries and the remaining vessels (noncapillaries) on the basis of a diameter threshold. Vessels with a diameter < 8 µm were considered to be capillaries. A threshold of 8 µm is an appropriate standard value well within the range of values used in other studies (Stewart et al. 1997; Michaloudi et al. 2005, and references therein).

For a semiquantitative estimation of cell density, the DAPI images were converted into 8-bit gray values and the gray values were taken as a relative measure of cell density (including all cell types). This analysis was restricted to V1.

Layer-specific ROIs (for the striate cortex: layers I, II, III, IVa, IVb, IVc-α, IVc-β, V, VI; for the extrastriate cortex: layers I, II/III, IV, V, VI) were drawn manually on the corresponding DAPI image (Fig. 3*B*) and were confirmed on the consecutive Nissl (Fig. 3*A*) and myelin stains. The mean depth of the center of mass of each layer-specific ROI is shown in Figures 4 and 5. Differences between area- and layer-specific measures were statistically analyzed using analyses of variance (ANOVAs) and Tukey post hoc tests using SPSS (SPSS, Inc., Chicago, IL). For comparisons between striate and extrastriate cortex, an ROI was drawn in V1 including all layer IV subdivisions and layers II and III were pooled.

COX Staining

Three animals were perfused as described above, with all consecutive steps kept as short as possible to preserve maximal obtainable oxidase activity. The visual cortices were dissected immediately after removal of the brain and cryoprotected in 10%, 20%, and 30% sucrose solution

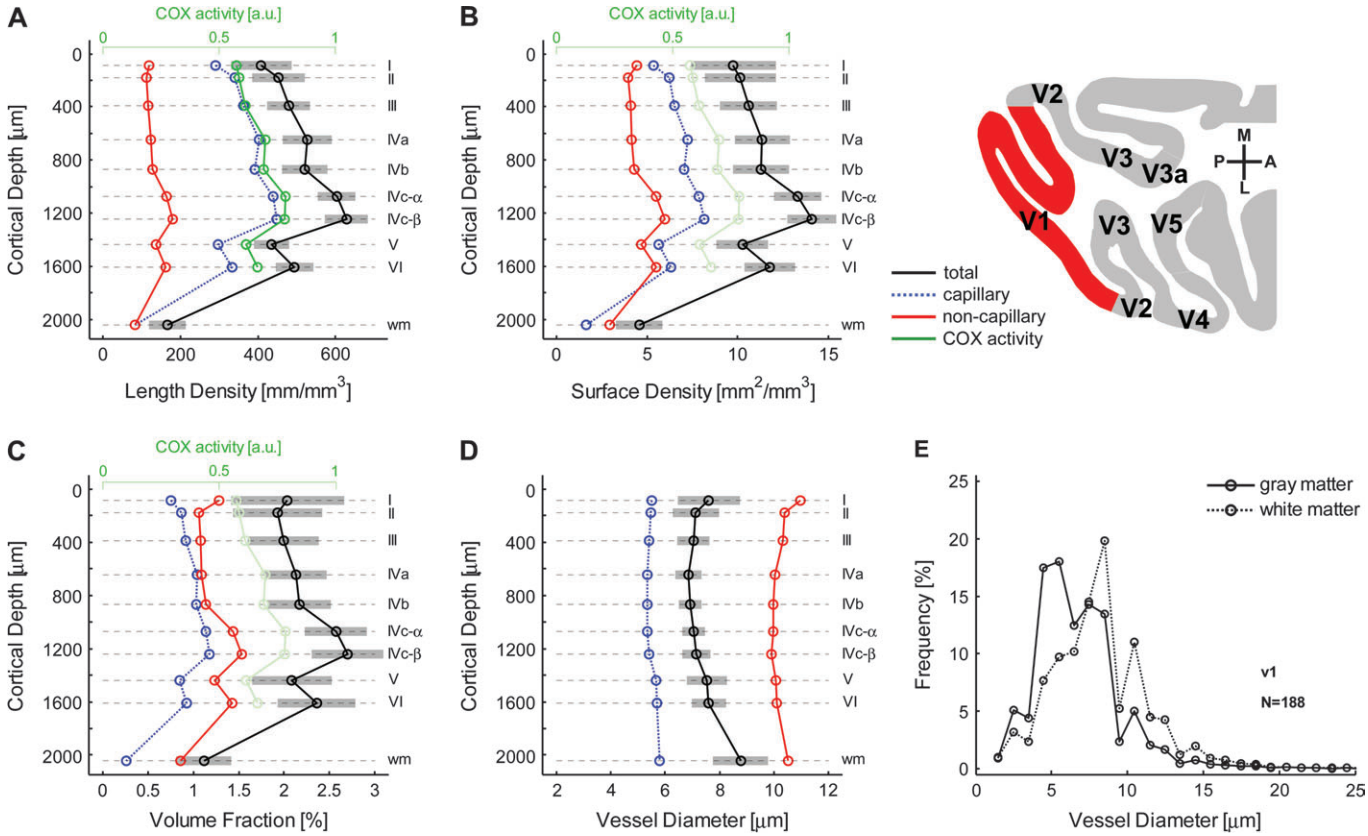

Figure 4. Lamina- and area-specific vascular density in visual area V1. Quantitative values of microvascular system across the cortical layers and cortical depths (µm from cortical surface) in the striate cortex. The black traces show the overall mean density (±standard deviation indicated with gray shaded area). The blue trace shows the values for the capillaries and the red for the noncapillary vessels. The green trace represents the COX activity in arbitrary units. Data for the microvascular parameters and the COX activity stem from different animals. (*B* and *C*) The COX data shown in (*A*) are replotted with transparent lines and symbols to facilitate comparison while affecting legibility as little as possible. (*A*) Length density in mm/mm^3. (B) Surface density in mm^2/mm^3. (*C*) Volume fraction in percent. (*D*) Average vessel diameters in µm. (*E*) Frequency distribution of vessel calibers for gray and white matter.

until they sank and then 60-µm-thick sections were cut horizontally. The sections were further processed for cytochrome *c* oxidase staining (Wong-Riley 1979, 1989; Wong-Riley and Welt 1980; Carroll and Wong-Riley 1984), and the rest of the brains were stored in 4% PFA. After washing in 0.1 M PB, the sections were incubated free floating and with light agitation at 37 °C in a solution consisting of 0.05% DAB (3,3′ diaminobenzidine tetrahydrochloride), 0.04% cytochrome *c* from horse heart, and 3% sucrose (all from Sigma) in 0.1 M PB under regular visual control until sufficient contrast was achieved. The reaction was stopped with 3 subsequent washing steps in 0.1 M PB and the sections were then mounted and cover-slipped as described above for the immunohistochemically stained sections.

Images were acquired using a microscope (Axiophot, 5× objective; Carl Zeiss, Göttingen, Germany) equipped with a CCD camera (Axiocam MRm, controlled by Axiovision 4.3; Zeiss, Göttingen, Germany). The images were converted into 8-bit gray values, the inverted gray values of the cortex were taken as a relative measure for oxidative metabolism (Wong-Riley 1979, 1989; Wong-Riley and Welt 1980; Carroll and Wong-Riley 1984). In V1, layer-specific ROIs were defined visually on the COX stains and were confirmed on the consecutive Nissl stain. The relationship between the layer-specific vascular densities and the cytochrome activities was statistically tested using the Spearman rank correlation.

Results

Corrosion Casts

The general organization of the cortical vasculature as described thoroughly by Duvernoy et al. (1981) in the human brain can also be identified in the vascular casts from the macaque monkey brain (see Figs 1 and 2). Large vessels are localized on the surface of the brain and the cortical arteries and veins are oriented perpendicular to the surface. Arteries are easily identified by their elongated imprints of the endothelial cell nuclei. These imprints appear more circular in the case of venous vessels. Large penetrating arteries were more numerous than veins; the ratio was found to be 1:~1.6 (number of identified vessels: 249). The total area of the analyzed tangential views was 33.7 mm^2. By dividing this area by the number of penetrating large vessels (132 arteries and 82 veins), we were able to determine the mean area irrigated or drained by the vessels to be 0.26 and 0.41 mm^2 for arteries and veins, respectively. Assuming a cylindrical volume and a mean cortical thickness of 1.7 mm, we can estimate an average irrigation volume of 0.44 mm^3 for large penetrating arteries and an average draining volume of 0.70 mm^3 for large cortical veins.

The cortical arteries themselves branch and give rise to a fine capillary network also called the capillary bed. The vascular density is markedly higher in gray than in white matter. However, within the cortex a continuous orderly pattern can be observed with only moderate changes in vascular density. Figure 2 shows the so-called plastic strips around arteries that have been reported by several authors (Castenholz et al. 1982; Aharinejad et al. 1990; Rodriguez-Baeza et al. 1998). As described before, these structures are not tightly connected to the vessel lumen (Fig. 2*B*). Most of these perivascular

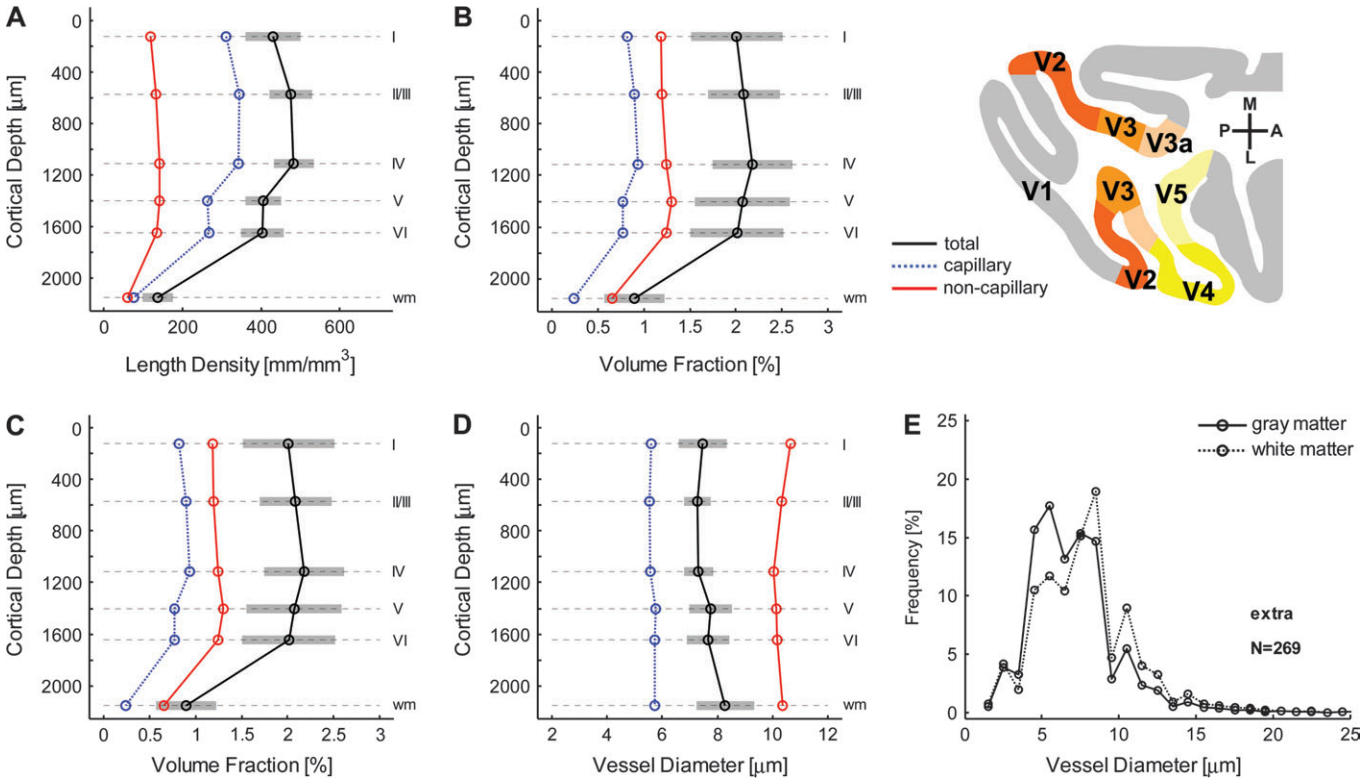

Figure 5. Quantitative values of microvascular system across the cortical layers and cortical depths (µm from cortical surface) in the extrastriate cortex. The black traces show the overall mean density (±standard deviation indicated with gray shaded area). The blue trace shows the values for the capillaries and the red for the noncapillary vessels. (A) Length density in mm/mm^3. (B) Surface density in mm^2/mm^3. (C) Volume fraction in percent. (D) Average vessel diameters in µm. (E) Frequency distribution of vessel calibers for gray and white matter.

structures can be found near the cortical surface and near arterial branching points. Circular constrictions from sphincter-like structures could not be identified with confidence. In very rare cases, a local and sudden decrease in the lumen could be detected; however, it was difficult to differentiate this with confidence from a locally incomplete filling.

Histochemistry

Using digital image processing and stereological analyses of the double histochemically stained sections (Fig. 3), we were able to derive several quantitative measures of the vascular system, including the length density (mm/mm^3), volume fraction (%), surface density (mm^2/mm^3), and mean vessel diameter (µm). A summary of the analysis is shown in Table 1. A total of 459 cortical samples were analyzed throughout the visual cortex (V1 n = 188; V2 n = 78; V3 n = 106; V4 n = 53; V5 n = 34). The mean vascular length density of gray matter in the visual cortex (n = 459) was 478.27 mm/mm^3, whereas the mean volume fraction was 2.14%, and the surface density was 10.97 mm^2/mm^3.

Layer-Specific Analysis of Vascular Density

Significant differences in vascular density measures (length density, volume fraction, and surface density) across cortical layers were observed in all areas investigated (ANOVAs for repeated measures: length density $F_{4/451}$ = 327.7, P < 0.001; volume fraction $F_{4/451}$ = 44.8, P < 0.001; surface density $F_{4/451}$ = 116.2, P < 0.001).

In V1, the vascular density was highest in layer IVc-β (Fig. 4, *A*: volume fraction 2.70%; *B*: length density 627.83 mm/mm^3; *C*: surface density 14.09 mm^2/mm^3). The lowest vascular length and surface density was found in layer I (*B*: length density 408.44 mm/mm^3; *C*: surface density 9.76 mm^2/mm^3), whereas layer 2 showed the lowest volume fraction (*A*: volume fraction 1.93%). Pairwise comparisons of the length densities between layers in V1 revealed significant differences (P < 0.05, Bonferroni-corrected for multiple comparisons) between all layers except between layer IVa and IVb. A summary of the pairwise comparisons between layers in V1 is given in Table 2.

In extrastriate cortex (pooled data V2, V3, V4, and V5, n = 271), layer IV showed the highest vascular density (Fig. 5, *A*: volume fraction 2.18%; *B*: length density 482.98 mm/mm^3; *C*: surface density 11.11 mm^2/mm^3) and layer VI the lowest (Fig. 5, *A*: volume fraction 2.01%; *B*: length density 403.71 mm/mm^3; *C*: surface density 9.74 mm^2/mm^3). Pairwise comparisons of the length density revealed significant differences (P < 0.05, Bonferroni-corrected for multiple comparisons) between all the layers. Similarly, in terms of volume fraction most of the layers were significantly different from each other, except for layers I and V, layers I and VI, and layers II/III and V. A summary of these pairwise comparisons is given in Table 3.

Analysis of Vessel Diameter

In V1 and in the extrastriate cortex, the mean diameter (see Figs 4*D* and 5*D*) differed across the cortical layers ($F_{4/451}$ = 62.6, P < 0.001, pooled data V1–V5). The overall mean diameter was 7.30 µm; the largest diameter (7.66 µm) was found in layer V and the smallest in layer IV (7.18 µm).

The frequency distributions of the vessel calibers for gray and white matter are given in Figures 4*E* and 5*E*. The small

Table 1
Area-specific quantification of microvascular system

	Length density (mm/mm^3)			Surface density (mm^2/mm^3)			Volume fraction (%)			Diameter (μm)		
	Total	Cap	Noncap	Total	Cap	Noncap	Total	Cap	Noncap	Total	Cap	Noncap
V1	512.03 (40.08)	373.92	138.11	11.50 (1.11)	6.80	4.70	2.22 (0.32)	0.97	1.24	7.15 (0.44)	5.43	10.16
V2	453.30 (43.28)	323.95	129.35	10.45 (1.40)	6.02	4.43	2.06 (0.42)	0.87	1.19	7.32 (0.52)	5.56	10.26
V3	460.56 (35.70)	324.95	135.61	10.78 (1.20)	6.08	4.70	2.11 (0.37)	0.86	1.25	7.44 (0.45)	5.59	10.37
V4	437.82 (38.06)	303.61	134.20	10.25 (1.12)	5.70	4.55	2.03 (0.34)	0.83	1.20	7.45 (0.44)	5.61	10.16
V5	467.15 (62.20)	322.95	144.19	10.91 (1.75)	6.00	4.92	2.14 (0.42)	0.85	1.29	7.42 (0.44)	5.56	10.22

Note: The overall mean (total) is shown with standard deviation in brackets as well as the corresponding contribution of capillaries (cap) and noncapillaries (noncap).

caliber vessels, particularly the capillaries with a diameter around 5 μm are clearly the most frequent vessels. A shift toward larger vessels with a considerable drop in capillary frequency can be seen in white matter.

Area-Specific Analysis of Vascular Density

When comparing the vascular density across the areas of the visual cortex, V1 was found to reach the highest levels of vascularization (see Table 1). Pairwise comparisons between V1 and all the other visual subareas revealed a significantly higher length density in V1 (univariate ANOVA, Tukey post hoc tests, $P < 0.05$). No significant differences were found within the extrastriate visual areas except for V4, which showed a slightly lower length density than all other areas (univariate ANOVA, Tukey post hoc tests, $P < 0.05$). The volume fraction was also highest in V1, however, the differences failed to reach significance in the comparisons between V1 versus V3 and V1 versus V5 (univariate ANOVA, Tukey post hoc tests, $P < 0.05$). There was no difference in volume fraction within the extrastriate areas. Similar results were obtained for the surface density, where the density was significantly higher than in all the extrastriate areas except for V5. Again, no difference was detected within the extrastriate areas. The mean vessel diameter was significantly smaller in V1 than in all other visual areas, and no significant differences were found within these extrastriate regions (univariate ANOVA, Tukey post hoc tests, $P < 0.05$).

When comparing individual layers between the visual areas, it was found that the length density of layer IV and layer VI in V1 was significantly higher than in all the extrastriate cortices (univariate ANOVA, Tukey post hoc tests, $P < 0.05$). This was also true for the volume fraction and surface density, however, the comparisons betweens V1 and V5 failed to reach significance for these measures.

Contribution of Capillaries and Noncapillaries

As demonstrated in Figures 4 and 5, the capillaries contribute differentially to the different vascular density quantities. When focusing on the mere length as in length density, it is obvious that by far the largest contribution is provided by the capillaries. However, for other quantities the contribution of the noncapillaries may be higher, according to their respective dependence on the vessel radius (the length density's dependence on the vessel diameter is d^0, that of the surface density is d^1 and that of the volume fraction is d^2). Due to the volume fraction's quadratic dependence on the diameter, the contribution of large vessels surpasses that of the capillaries, despite their much lower frequency. It is important to note that the threshold for the differentiation between capillaries and noncapillaries has a large impact on these measures (details are given in the Appendix and in the Supplementary Fig. 1).

COX Activity

A total of 89 cortical samples from V1 were analyzed. The COX staining shows the well-known characteristic laminar pattern in V1 (Fig. 6). The laminar profile of the semiquantitative COX activity can be seen in Figure 4; it is very obvious that it strictly follows the vascular density. The correlation between vascular density and COX activity proved to be significant, particularly for the capillary vascular density measures (Fig. 6). The correlation coefficients between the vascular density and COX activity across layers were found to be around 0.9 for capillary density (see Fig. 6).

Cell Density

The DAPI images yielded a relative measure of cell density. The layer-specific correlation between cell density and vascular density in V1 revealed a weak relationship in the upper cortical layers. In deeper layers the 2 densities are clearly more closely correlated (Fig. 6 and Supplementary Fig. 2). When all the layers are considered, only the correlation between the capillary length and surface density and the cell density proved to be significant.

Discussion

Qualitative Aspects as Assessed by the Corrosion Cast Technique

To our knowledge, this is the 1st study applying the corrosion cast technique to investigate the cerebral vasculature in the macaque monkey. As expected, the general organization of the cerebral vasculature is very similar to that described for other species (e.g., the human Duvernoy et al. 1981; Reina-De La Torre et al. 1998).

We were able to detect abundant perivascular structures. These ring-like structures were only found around arteries, and were most frequently located near the surface of the cortex or before or after arterial branching points. Although the origin of these structures is still debated (Castenholz et al. 1982; Aharinejad et al. 1990; Rodriguez-Baeza et al. 1998), we favor the hypothesis that they originate from resin being pushed into space normally occupied by arterial smooth muscles. A reason for this could be that in the process of perfusion, fixation, and/or resin injection, the tight junctions at the endothelial cells are ruptured at certain locations. Circular constrictions from sphincter-like structures, as described by others (Rodriguez-Baeza et al. 1998; Harrison et al. 2002), could not be detected in our samples. It is important to note that these constrictions should also be visible in the basal membrane, that is, in the anticollagen stain. Taken together, using both immunostaining of the basal membrane as well as corrosion casts, we were

Table 2
Laminar differences in V1

Length Density [Δ in %]

	I	II	III	IVa	IVb	IVca	IVcb	V	VI
I		10.8	17.1	28.8	27.4	47.6	53.7	6.1	20.8
II			5.7	16.3	15.0	33.3	38.7	-4.2	9.0
III				10.0	8.8	26.0	31.2	-9.4	3.1
IVa					-1.1	14.6	19.3	-17.6	-6.3
IVb						15.9	20.6	-16.7	-5.2
IVca							4.1	-28.1	-18.2
IVcb								-30.9	-21.4
V									13.8
VI									

Volume Fraction [Δ in %]

	I	II	III	IVa	IVb	IVca	IVcb	V	VI
I		-5.4	-2.2	4.3	6.2	26.1	32.4	2.1	15.5
II			3.4	10.3	12.3	33.4	40.0	7.9	22.1
III				6.6	8.6	29.0	35.4	4.4	18.0
IVa					1.9	20.9	27.0	-2.1	10.7
IVb						18.7	24.7	-3.9	8.7
IVca							5.0	-19.1	-8.5
IVcb								-22.9	-12.8
V									13.1
VI									

Surface Density [Δ in %]

	I	II	III	IVa	IVb	IVca	IVcb	V	VI
I		3.8	8.5	16.1	15.8	36.7	44.3	4.9	20.6
II			4.4	11.8	11.5	31.7	38.9	1.1	16.1
III				7.1	6.8	26.1	33.0	-3.2	11.2
IVa					-0.3	17.7	24.2	-9.6	3.8
IVb						18.1	24.6	-9.4	4.1
IVca							5.5	-23.2	-11.8
IVcb								-27.3	-16.4
V									14.9
VI									

Note: Laminar differences in length density, volume fraction, and surface density. The differences between 2 laminae are shown in percent. Gray shaded areas indicate differences that did *not* reach statistical significance.

Table 3
Laminar differences in extrastriate cortex

Length Density [Δ in %]

	I	II/III	IV	V	VI
I		10.6	12.4	-5.9	-5.9
II/III			1.6	-14.9	-15.0
IV				-16.3	-16.3
V					-0.1
VI					

Volume Fraction [Δ in %]

	I	II/III	IV	V	VI
I		4.0	8.7	3.3	0.3
II/III			4.5	-0.7	-3.5
IV				-5.0	-7.7
V					-2.9
VI					

Surface Density [Δ in %]

	I	II/III	IV	V	VI
I		8.1	10.5	-1.9	-3.2
II/III			2.1	-9.3	-10.5
IV				-11.2	-12.3
V					-1.3
VI					

Note: Laminar differences in length density, volume fraction, and surface density. The differences between 2 laminae are shown in percent. Gray shaded areas indicate differences that did *not* reach statistical significance.

unable to detect a relevant number of constrictions. It is obvious that the presence or absence of such constrictions depends on the tone of the smooth muscles and pericytes surrounding the vessel and that this muscle tone is substantially influenced by the perfusion and fixation procedure. Therefore, it might be that these constrictions do exist in vivo, most likely in a constricted state by default in order to allow the increase of blood flow on demand, but that they are dilated in the course of perfusion and fixation.

Unlike others (Harrison et al. 2002), we were unable to detect apparent discontinuities in the vasculature. Instead, we found a homogeneously distributed vasculature along both the tangential and the in-depth direction of cortex. This is also what one would expect, because the intercapillary mesh size is most likely determined by the diffusion coefficient of oxygen, which is approximately 50 μm in gray matter. A discontinuous

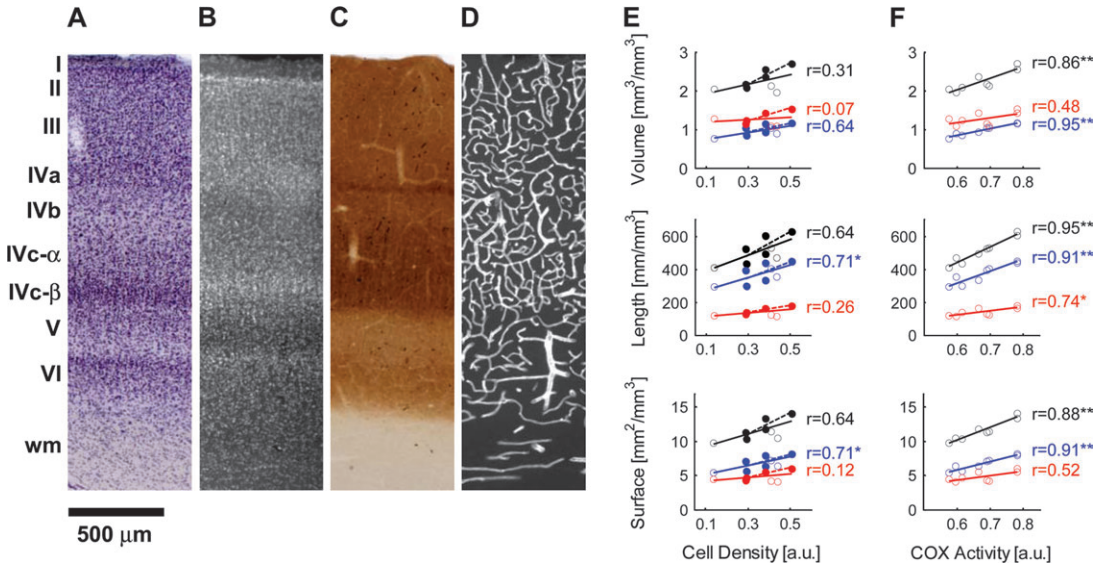

Figure 6. COX activity and cell density in V1. Representative Nissl (*A*), DAPI (*B*), COX (*C*), and anticollagen stain (*D*) of V1 section showing the characteristic laminar pattern of the area. The relationship between cell density and vascular density is shown in (*E*). In the lower cortical layers (layers IV, V, and VI; represented by solid circles and dashed regression line) the correlation is stronger than in the upper layers (layers I, II and III; represented by open circles). The level of basal oxidative metabolism as measured by COX activity staining correlates well with the vascular density measures (*F*). The data represent the mean values from all layer-specific ROIs for the vascular density (*y*-axis) and COX activity (*x*-axis). The vascular data and the COX data were measured in different animals. The blue values represent the capillary and the red represent the noncapillary density, whereas the black traces are based on the total vascular density. The Spearman rank correlation coefficient is provided with its corresponding level of statistical significance (**$P<0.001$, *$P<0.01$).

vascular system as proposed by Harrison et al. (2002) would therefore probably fail to meet the high steady-state metabolic demand of the cortex. We believe that the main reason for the proposed discontinuity of the vasculature was an incomplete intravascular filling. Round or tapered dead ends are well-known indicators of incomplete intravascular filling (for an excellent review on the vascular corrosion cast method, see Lametschwandtner et al. 1990). One could argue that the incomplete filling is due to "physiologically" closed vessels, as suggested by the controversial capillary recruitment phenomenon (Gobel et al. 1989; Pinard et al. 2000). However, in the work of Harrison and colleagues many dead ends can be seen in large vessels for which a recruitment mechanism has never been proposed and can therefore be ruled out.

In spite of their undisputed usefulness for the *qualitative* assessment of the vasculature with great detail (e.g., differentiation between arteries and veins, demonstration of perivascular structures) reliable *quantitative* volumetric data from corrosion casts are difficult to acquire. It is important to note that the technical difficulties become even more pronounced in larger animals such as the macaque monkey. Another disadvantage of the corrosion cast technique is that the tissue is lost due to the maceration process, which renders an exact localization within or between areas impossible. Therefore, we chose to supplement it with a histological approach for an exact layer- and area-specific quantification of the vasculature in the macaque visual cortex.

Quantitative Aspects as Assessed by Immunohistochemistry

One can assume that the density of the vascular network is optimized for a number of parameters. For example, the network has to be dense enough to make sure that diffusion of oxygen and transport of energy substrates are in register with the enormous metabolic activity of brain tissue. On the other hand, the network has to be sparse enough to comply with space and cost limitations. To our knowledge, this is the 1st quantitative study of the macaque cerebral microvasculature (quantitative in the strict sense, i.e., providing density values with units such as mm/mm^3). The vascular density values were stereologically determined on the basis of anticollagen immunohistochemistry from a large number of samples. Although the absolute values have to be treated with a certain amount of caution (see methodological remarks), they are well within the range of earlier studies performed in other species and using different methods. The overall vascular length density in visual gray matter lies around 478 mm/mm^3, whereas the volume fraction is approximately 2.1%.

It is important to note that the computed density variables (length density, surface, and volume fraction) are not strictly independent. They depend differently on the mean vascular diameter of a given region (consult the Appendix for a more comprehensive consideration of this issue). At any rate, because all 3 variables have distinct physiological implications it seemed appropriate to present each of them separately.

Area-Specific Vascular Density

It has been described before that the primary visual cortex seems to be unique with respect to the microvascular system as well (Zheng et al. 1991; Fonta and Imbert 2002; Tieman et al. 2004). Overall vascular density is clearly higher in the striate cortex than in the extrastriate cortices. One novel finding of the present study was the fact that the differences within the several extrastriate areas were small or even negligible. Interestingly, the difference between the primary and non-primary areas was also found in the somatosensory and auditory cortex (data not shown), and again, the vascular densities of the secondary auditory and somatosensory areas were comparable with those of the extrastriate cortex. A detailed quantitative description of the nonvisual areas would clearly be beyond the

scope of the present work and will be presented elsewhere. Taken together, it seems that nonprimary areas share the same microvascular architecture. From a mere structural point of view large differences in the hemodynamic response are not to be expected within these areas. However, our results clearly suggest that caution is advised when hemodynamic response patterns are compared between primary and nonprimary areas.

Layer-Specific Vascular Density

In the primary visual cortex, we found a marked gradient in the microvascular density along the cortical layers, with the highest density in layer IVc-β. This is in agreement with studies in the squirrel monkey (Zheng et al. 1991) and the marmoset (Fonta and Imbert 2002). In a semiquantitative study, Fonta and Imbert (2002) were able to demonstrate that the relative vascular density developed in parallel to COX activity and was highest in layer IVc-α in the 1st postnatal month. Shortly afterward the 2 layers match in vascular density and COX activity, before layer IVc-β eventually becomes the most densely vascularized layer. In the cat, a similar change in steady-state metabolic demand and vascular density was observed. It was found that layer IV in the cat striate area 17 showed the highest relative vascular density and relative glucose utilization. However, this laminar difference could only be found in the adult but not in 5-week-old kittens (Tieman et al. 2004).

As shown in other species the extrastriate cortex exhibits a lower vascular density than the primary visual area (Duvernoy et al. 1981; Zheng et al. 1991; Tieman et al. 2004) and the laminar differences are clearly less pronounced, a result that is also seen when comparing laminar differences in cell and synapse densities. Furthermore, the laminar differences are very similar within the subareas of the extrastriate cortex.

Length Density versus Volume Fraction

It is interesting to note that in general, differences in length density were more pronounced than differences in volume fraction (be it between layers or areas). As an example, V1 has an overall length density that is 11% higher than in V2, whereas the difference in volume fraction is only 7%. Moreover, the mean diameter of the vessels is somewhat lower in V1 than in V2. Taken together, these results indicate that the capillary rather than the overall vascular density is increased in order to match the needed supply of oxygen and energy substrates. In principle there are 2 ways to increase capillary density, namely capillary proliferation and capillary segment elongation (Mironov et al. 1994). However, to differentiate these 2 mechanisms, 3-dimensional data acquisition is mandatory, for example, using either confocal microscopy (Cassot et al. 2006) or synchrotron-radiation based x-ray microscopy (srXTM) (Plouraboue et al. 2004; Heinzer et al. 2006). Our own preliminary data obtained from srXTM clearly indicate a greater contribution of an increased number of capillaries as opposed to an increase in capillary segment length or tortuosity (data not shown). In hypobaric hypoxia, it was shown that the opposite is the case, indicating that in acute situations the brain reacts with capillary segment elongation (Mironov et al. 1994).

Methodological Issues

The anticollagen staining and subsequent image processing proved to be an adequate approach that provides density measures that are within the range of previously published data from other species and/or cortical areas. However, there are certain methodological issues that need to be addressed. First, the overall volume fraction is lower than that derived from other methods, such as positron emission tomography using CO inhalation. One of the reasons for this could be that the large pial vessels (see corrosion cast images in Fig. 1) are not included in our immunohistochemical data. Furthermore, some large vessels are lost during the processing of the sections. Although the large vessels are scarce, they contribute considerably to the vascular volume, as elaborated above. The segmentation process that eventually yields the binarized vessel data, of course, considerably influences the quantified vascular density values. Although great care was taken to optimize this process, one has to be aware that some error is to be expected, as in most fully quantitative studies. Our preliminary data using synchrotron-based X-ray microscopy confirm the density values presented in this study. Future work will profit considerably from this new technology, because it can produce true volumetric data from a large field of view with sufficient resolution. Tomographic methods will be the basis of required investigations of the vascular network topology in physiology and pathology.

One of the major drawbacks of the applied immunohistochemical method is the inability to differentiate between arterial and venous vessels, which was possible using the corrosion cast technique. There are several studies that suggest specific antibodies for either arteries or veins, at least in the developing and unfixed brain tissue (e.g., smooth muscle actin, eph, ephrin). We have screened these antibodies but we were unable to produce satisfying results in the adult well-fixed macaque brain.

Vascular Density: Correlation with Element Density or Regional Metabolic Activity?

An important issue concerns the covariation of vascular density with the density of neurons, synapses and glia. The fact that perisynaptic elements are the most costly in terms of energy metabolism (Mata et al. 1980; Erecinska and Dagani 1990; Jueptner and Weiller 1995) would argue in favor of a tighter relationship between vascular density and the synaptic rather than the neuronal density (Logothetis and Wandell 2004). Interestingly, the data we present here show that this assumption is wrong. In fact, correlating the layer-specific densities of neurons, synapses, and glia from the literature (O'Kusky and Colonnier 1982; Bourgeois and Rakic 1993) with the vascular density of the present data suggests that the correlation between the synaptic and vascular density is very weak (see Supplementary Fig. 3), particularly because layers II and III show a high synaptic but rather low vascular density. For the upper cortical layers, the correlation between our semi-quantitative cell density measure and the vascular density proved to be rather weak. Furthermore, neuronal density measures taken from the literature (O'Kusky and Colonnier 1982; Bourgeois and Rakic 1993) did not correlate significantly with the vascular density assessed in the present study. Taken together, these facts indicate that there is a weak positive correlation between cellular (particularly neuronal) density and vascular density. However, when focusing on layer I, it becomes obvious that these relationships are not straightforward. As described by others, layer I exhibits an extremely low neuronal density, and there the vascular density is clearly more closely related to the synaptic density (Duvernoy et al. 1981). The comparison between the vascular data and the values for

the cellular (own data and from literature) and synaptic density (from literature) provide an adequate 1st approximation of this important relationship. Measuring the synaptic and cellular densities in identical samples is a mandatory next step, although our existing data together with the observation briefly discussed in the next paragraph suggest that element density and vascular density need not necessarily be strongly correlated in a system optimizing the coupling of steady-state neuronal activity with its supply of energy.

In particular, to better understand the underlying reasons for vascular density distribution, we used an established methodology (COX) to measure the regional energy consumption in the same cortical areas of different animals. In contrast to the weak correlations with synaptic density and cellular densities (in upper cortical layers) we found a tight relationship between metabolic demand and vascular density. Correlations between the layer-specific COX activity and the capillary density measures were very strong in V1. This is in agreement with earlier studies, although most of them did not investigate the relationship in a strictly quantitative way (Zheng et al. 1991; Cox et al. 1993; Riddle et al. 1993; Woolsey et al. 1996; Fonta and Imbert 2002; Tieman et al. 2004). Techniques such as the 2-deoxyglucose method would be more effective for quantitatively assessing the metabolic rate. Yet, the remarkable relationship between the measured vascular density and the semiquantitative COX activities indicates that the use of the method in this study is justified, at least as a 1st approximation.

Strictly speaking, the fact that the vascular density correlates well with the steady-state metabolic demand is hardly surprising. What is interesting, and perhaps unexpected, is rather the dissociation of energy demand and element density in cortex. We speculate that this dissociation reflects the degree of differentiated integration of a cortical area. A typical pyramidal cell in the primate cortex receives approximately 10 000 inputs, and a column underneath 1 mm^2 in the visual cortex has approximately 200 000 neurons (Braitenberg and Schuez 1998). Given the weak thalamic input in any cortical area (approximately 10–15% of the area's total input), these very large numbers suggest a context-dependent integration of information, according to which regional processing probably never reflects the activation of all synapses and cells at any given time in life. Instead, the steady-state energy demands follow the default functional mode of the system, which might in turn echo the average feedforward input to an area together with the average neuromodulatory effects of the ascending diffuse systems. Effects related to cognitive states or to different types of sensory–motor integrative actions may be entirely context-dependent and not co-occurring; in other words the number of regional elements might never be recruited at the same time. If so, element density reflects a region's capacity to process information, whereas vascular density and energy consumption reflect the minimal processes that are instantiated in the region's idling state. Finally, the explanation of the fact that the laminae IV–VI displayed a much closer relationship between cell density and vascular density than the upper layers is subject to future research, which will have to include data of cell type–specific densities.

Implications for Functional Imaging Based on Hemodynamic Responses

It is evident that the understanding of the signals originating from noninvasive functional neuroimaging modalities such as functional magnetic resonance imaging in part relies on a profound knowledge of the cerebrovascular structure (Turner 2002). The quantitative analysis of the area- and layer-specific vascular density is a 1st important step and will provide important information for theoretical considerations that in part rely on such values. For example, many models of the BOLD signal require the blood volume fraction as an a priori parameter (Buxton et al. 1998, 2004) and it has so far been disregarded that differences might exist within or between cortical areas. One ultimate goal would be to estimate a vascular point spread function (Logothetis and Wandell 2004; Weber et al. 2004; Sheth, Nemoto, Guiou, Walker, Pouratian, Hageman, et al. 2004; Dunn et al. 2005; Sheth et al. 2005) on the basis of the vascular structure. To achieve this, the density of the blood-flow-regulating structures has to be known. This would—above all—involve the differentiation of arteries from veins, because the smooth muscle sheath around the arteries is a key player in regulating the vascular resistance. Furthermore, the density of all other contractile elements, such as sphincter-like perivascular structures (Rodriguez-Baeza et al. 1998) or pericytes (Peppiatt et al. 2006) has to be assessed. The corrosion cast data provide clear evidence that the draining volume of large penetrating cortical veins is considerably larger than the feeding territory of a penetrating cortical artery. It was recently shown that these arteries can be considered a bottleneck in the feeding system, because photothrombosis of individual vessels of this type leads to a severe disruption of perfusion in an area extending as far as 350 μm in radius (Nishimura et al. 2007). One of the most frequently used imaging sequences in BOLD fMRI—gradient echo echo-planar imaging (EPI)—is sensitive to local susceptibility gradients, which originate predominantly near draining veins. On the basis of the present data, the ultimate spatial resolution of an imaging scheme based on the penetrating venous vessels would be around 0.70 mm^3. It is evident that imaging signals originating from arteries (feeding volume 0.44 mm^3) or even better from capillaries—such as spin-echo EPI—would provide a superior spatial resolution (Lee et al. 1999; Yacoub et al. 2003; Goense and Logothetis 2006; Harel et al. 2006; Goense et al. 2007).

A better and more quantitative understanding of cerebral blood flow control could be obtained through fluid dynamic modeling. For this purpose, *tomographic* assessments of the vasculature in large cortical fields of view are necessary to obtain the 3-dimensional topology of the vascular network, using the currently available methods mentioned above (Plouraboue et al. 2004; Cassot et al. 2006; Heinzer et al. 2006).

The fact that the microvascular system of the primary visual cortex (and also the primary somatosensory and auditory cortices) is clearly different from the nonprimary regions has direct and important implications for functional neuroimaging studies. Although the influence of vascular density on the hemodynamic response is a subject for further research, caution is advised in studies that draw conclusions from differential signals measured in primary versus nonprimary cortical areas. It might be argued that a higher microvascular density causes an increased signal-to-noise ratio of the hemodynamic signals and consequently increases the chances of detecting differences between conditions.

Supplementary Material

Supplementary material can be found at: http://www.cercor.oxfordjournals.org/.

Funding

Max Planck Society; Schweizerische Stiftung für biologisch-medizinische Studien SSMBS; and by the Swiss National Science Foundation (PP00B—110751/1).

Notes

We thank Almut Schüz, Heinz Schwarz, Gregory J. del Zoppo for their help with the immunohistochemical procedures and for important discussions as well as Denis Chaimow for stereological suggestions.

Conflict of Interest: None declared.

Address correspondence to Bruno Weber, Institute of Pharmacology and Toxicology, University of Zürich, Rämistrasse 100, 8091 Zürich and Nikos Logothetis, Max Planck Institute für biologische Kybernetik, Spemannstr. 38, 72076 Tübingen, Germany.

Appendix

As illustrated in Figure 3, the raw anticollagen images can be thresholded and binarized, yielding an area fraction A_F. The parameters for the image processing were kept constant for all samples. It is obvious that the choice of the threshold significantly influences the resulting A_F. The parameters were carefully set in order to optimize the match between the raw image (Fig. 3*E*) and the binarized image (Fig. 3*F*). This optimization was guided by visual inspection. By eroding the binarized images to single lines, we were able to produce the eroded area fraction E_F (Fig. 3*G*). From A_F, E_F and the remaining known quantities (pixel width a_{pix} and slice thickness t), the length density L_V, the surface density S_V, and volume fraction V_V of the blood vessels can be derived.

Area Fraction

The area fraction A_F is defined as the quotient of the total projected vessel area and the total area of the projection A_{total}. If we approximate the vascular tree by a network of cylinders i with lengths l_i and diameters d_i, we can write

$$A_F = \frac{\sum_i l_{pi} d_i}{A_{total}} = \frac{\sum_i f_i l_i d_i}{A_{total}} = f \frac{\sum_i l_i d_i}{A_{total}} \quad (1)$$

Here, f_i is the ratio of projected and true vessel lengths. In the last step it was assumed that this factor is uniform across all vessels.

As the projection image is not continuous, but consists of pixel elements, the projected area in the pixel image A_F^{pix} will differ from the true projected area by a factor p_A.

Thus,

$$A_F^{pix} = A_F p_A = f p_A \frac{\sum_i l_i d_i}{A_{total}} = f p_A \frac{\sum_i l_i d_i}{N_{pix} a_{pix}^2}, \quad (2)$$

where N_{pix} denotes the total number of pixels in the projection image. The lengths l_i in the pixel image are multiples of the pixel-length a_{pix}.

Eroded Area Fraction

Analogous to A_F, the eroded area fraction E_F can be calculated by

$$E_F = \frac{\sum_i l_{pi} d_u}{A_{total}} = \frac{\sum_i f_i l_i d_u}{A_{total}} = f d_u \frac{\sum_i l_i}{A_{total}} \quad (3)$$

where d_u is the unit diameter.

The pixel image will introduce an additional factor p_E, yielding

$$E_F^{pix} = E_F p_E = f d_u p_E \frac{\sum_i l_i}{A_{total}} = f a_{pix} p_E \frac{\sum_i l_i}{N_{pix} a_{pix}^2} \quad (4)$$

Equations (1–4) do not take into account crossings of blood vessels in the projection image and therefore the present study slightly underestimates the projected length.

Length Density

The length density L_V of the blood vessels in the volume V_{total} is given by

$$L_V = \frac{\sum_i l_i}{V_{total}} = \frac{E_F A_{total}}{f d_u V_{total}} = \frac{E_F}{f d_u t} = \frac{4 E_F}{\pi d_u t} \quad (5)$$

In the last step an isotropic orientation of the vessels was assumed, resulting in $f = \pi/4$ (see also Russ and Dehoff 2000). The length density in the pixel image can thus be expressed as

$$L_V = \frac{4 E_F^{pix}}{\pi a_{pix} t p_E} \quad (6)$$

Surface Density

Just as the length density can be expressed in terms of the eroded area fraction, the area fraction can be used to calculate the surface density S_V.

$$S_V = \frac{\sum_i l_i \pi d_i}{V_{total}} = \frac{\pi A_F A_{total}}{f V_{total}} = \frac{\pi A_F}{f t} = \frac{4 A_F}{t} \quad (7)$$

The pixel image relates to S_V in the following way

$$S_V = \frac{4 A_F^{pix}}{t \quad p_A}. \quad (8)$$

Volume Fraction

The volume fraction V_F can be written as

$$V_F = \frac{\sum_i \pi \left(\frac{d_i}{2}\right)^2 l_i}{V_{total}} = \frac{\pi}{4 V_{total}} \sum_i d_i^2 l_i = \frac{\pi}{4 V_{total}} d_V \sum_i d_i l_i = \frac{S_V}{4} d_V = \frac{d_V A_F}{t}, \quad (9)$$

where d_V denotes a mean diameter. If we assume that $d_V = d_u A_F / E_F$, equation (9) becomes

$$V_F = \frac{d_u A_F^2}{t E_F}. \quad (10)$$

For a pixel image, the above relation will change to

$$V_F = a_{pix} \frac{\left(A_F^{pix}\right)^2 p_E}{t E_F^{pix} \quad p_A^2}. \quad (11)$$

Threshold Dependence of Capillary Contribution to Vascular Density

In addition to the overall quantification, we analyzed the data separately for capillaries and the remaining larger vessels (noncapillaries). Because capillaries cannot be differentiated qualitatively from other vessel types on the anticollagen stains, this differentiation had to be based on the caliber. We chose a threshold of 8 μm. It is obvious that the choice of this threshold greatly influences the relative contributions of capillaries and noncapillaries. To demonstrate this dependence, we computed the capillary and noncapillary length density, surface density and volume density, applying a range of thresholds. In Supplement Figure 1, capillary and noncapillary density measures are shown as a function of the threshold. It can easily be seen that the crossing of the capillary and noncapillary traces (i.e., equal contribution of the 2 vessel classes) shifts to the right with increasing dependence on the diameter (d^0 for length density, d^1 for surface density, d^2 for volume fraction).

References

Aharinejad S, Lametschwandtner A, Holtl W, Firbas W. 1990. The microvasculature of the guinea pig ureter. A scanning electron microscopic investigation. Scanning Microsc. 4:957–965; discussion 965–956.

Bourgeois JP, Rakic P. 1993. Changes of synaptic density in the primary visual cortex of the macaque monkey from fetal to adult stage. J Neurosci. 13:2801–2820.

Braitenberg V, Schuez A. 1998. Cortex, statistic and geometry of neuronal connectivity. Berlin: Springer.

Buxton RB, Uludag K, Dubowitz DJ, Liu TT. 2004. Modeling the hemodynamic response to brain activation. Neuroimage. 23(Suppl 1): S220–S233.

Buxton RB, Wong EC, Frank LR. 1998. Dynamics of blood flow and oxygenation changes during brain activation: the balloon model. Magn Reson Med. 39:855–864.

Carroll EW, Wong-Riley MT. 1984. Quantitative light and electron microscopic analysis of cytochrome oxidase-rich zones in the striate cortex of the squirrel monkey. J Comp Neurol. 222:1–17.

Cassot F, Lauwers F, Fouard C, Prohaska S, Lauwers-Cances V. 2006. A novel 3-dimensional computer-assisted method for a quantitative study of microvascular networks of the human cerebral cortex. Microcirculation. 13:1–18.

Castenholz A, Zoltzer H, Erhardt H. 1982. Structures imitating myocytes and pericytes in corrosion casts of terminal blood vessels. A methodical approach to the phenomenon of "plastic strips" in SEM. Mikroskopie. 39:95–106.
Cox SB, Woolsey TA, Rovainen CM. 1993. Localized dynamic changes in cortical blood flow with whisker stimulation corresponds to matched vascular and neuronal architecture of rat barrels. J Cereb Blood Flow Metab. 13:899–913.
Devor A, Dunn AK, Andermann ML, Ulbert I, Boas DA, Dale AM. 2003. Coupling of total hemoglobin concentration, oxygenation, and neural activity in rat somatosensory cortex. Neuron. 39:353–359.
Dunn AK, Devor A, Dale AM, Boas DA. 2005. Spatial extent of oxygen metabolism and hemodynamic changes during functional activation of the rat somatosensory cortex. Neuroimage. 27:279–290.
Duvernoy HM, Delon S, Vannson JL. 1981. Cortical blood vessels of the human brain. Brain Res Bull. 7:519–579.
Erecinska M, Dagani F. 1990. Relationships between the neuronal sodium/potassium pump and energy metabolism. Effects of K+, Na+, and adenosine triphosphate in isolated brain synaptosomes. J Gen Physiol. 95:591–616.
Fonta C, Imbert M. 2002. Vascularization in the primate visual cortex during development. Cereb Cortex. 12:199–211.
Fukuda S, Fini CA, Mabuchi T, Koziol JA, Eggleston LL, Jr, del Zoppo GJ. 2004. Focal cerebral ischemia induces active proteases that degrade microvascular matrix. Stroke. 35:998–1004.
Gobel U, Klein B, Schrock H, Kuschinsky W. 1989. Lack of capillary recruitment in the brains of awake rats during hypercapnia. J Cereb Blood Flow Metab. 9:491–499.
Goense JB, Logothetis NK. 2006. Laminar specificity in monkey V1 using high-resolution SE-fMRI. Magn Reson Imaging. 24:381–392.
Goense JB, Zappe AC, Logothetis NK. 2007. High-resolution fMRI of macaque V1. Magn Reson Imaging. 25:740–747.
Hamann GF, Okada Y, Fitridge R, del Zoppo GJ. 1995. Microvascular basal lamina antigens disappear during cerebral ischemia and reperfusion. Stroke. 26:2120–2126.
Harel N, Lin J, Moeller S, Ugurbil K, Yacoub E. 2006. Combined imaging-histological study of cortical laminar specificity of fMRI signals. Neuroimage. 29:879–887.
Harrison RV, Harel N, Panesar J, Mount RJ. 2002. Blood capillary distribution correlates with hemodynamic-based functional imaging in cerebral cortex. Cereb Cortex. 12:225–233.
Heinzer S, Krucker T, Stampanoni M, Abela R, Meyer EP, Schuler A, Schneider P, Muller R. 2006. Hierarchical microimaging for multiscale analysis of large vascular networks. Neuroimage. 32:626–636.
Jones M, Hewson-Stoate N, Martindale J, Redgrave P, Mayhew J. 2004. Nonlinear coupling of neural activity and CBF in rodent barrel cortex. Neuroimage. 22:956–965.
Jueptner M, Weiller C. 1995. Review: does measurement of regional cerebral blood flow reflect synaptic activity? Implications for PET and fMRI. Neuroimage. 2:148–156.
Kwong KK, Belliveau JW, Chesler DA, Goldberg IE, Weisskoff RM, Poncelet BP, Kennedy DN, Hoppel BE, Cohen MS, Turner R, et al. 1992. Dynamic magnetic resonance imaging of human brain activity during primary sensory stimulation. Proc Natl Acad Sci USA. 89:5675–5679.
Lametschwandtner A, Lametschwandtner U, Weiger T. 1990. Scanning electron microscopy of vascular corrosion casts—technique and applications: updated review. Scanning Microsc. 4:889–940; discussion 941.
Lee SP, Silva AC, Ugurbil K, Kim SG. 1999. Diffusion-weighted spin-echo fMRI at 9.4 T: microvascular/tissue contribution to BOLD signal changes. Magn Reson Med. 42:919–928.
Logothetis NK, Pauls J, Augath M, Trinath T, Oeltermann A. 2001. Neurophysiological investigation of the basis of the fMRI signal. Nature. 412:150–157.
Logothetis NK, Wandell BA. 2004. Interpreting the BOLD signal. Annu Rev Physiol. 66:735–769.
Martindale J, Berwick J, Martin C, Kong Y, Zheng Y, Mayhew J. 2005. Long duration stimuli and nonlinearities in the neural-haemodynamic coupling. J Cereb Blood Flow Metab. 25:651–661.
Mata M, Fink DJ, Gainer H, Smith CB, Davidsen L, Savaki H, Schwartz WJ, Sokoloff L. 1980. Activity-dependent energy metabolism in rat posterior pituitary primarily reflects sodium pump activity. J Neurochem. 34:213–215.
Michaloudi H, Grivas I, Batzios C, Chiotelli M, Papadopoulos GC. 2005. Areal and laminar variations in the vascularity of the visual, auditory, and entorhinal cortices of the developing rat brain. Brain Res Dev Brain Res. 155:60–70.
Miodonski A, Hodde K, Bakker C. 1976. Rasterelektronenmikroskopie von Plastik Korrosions Präparaten: morphologische Unterschiede zwischen Arterien und Venen. BEDO. 9:435–442.
Mironov V, Hritz MA, LaManna JC, Hudetz AG, Harik SI. 1994. Architectural alterations in rat cerebral microvessels after hypobaric hypoxia. Brain Res. 660:73–80.
Mosso A. 1881. Ueber den Kreislauf des Blutes im Menschlichen Gehirn. Leipzig: Von Veit.
Nishimura N, Schaffer CB, Friedman B, Lyden PD, Kleinfeld D. 2007. Penetrating arterioles are a bottleneck in the perfusion of neocortex. Proc Natl Acad Sci USA. 104:365–370.
O'Kusky J, Colonnier M. 1982. A laminar analysis of the number of neurons, glia, and synapses in the adult cortex (area 17) of adult macaque monkeys. J Comp Neurol. 210:278–290.
Ogawa S, Lee TM, Kay AR, Tank DW. 1990. Brain magnetic resonance imaging with contrast dependent on blood oxygenation. Proc Natl Acad Sci USA. 87:9868–9872.
Peppiatt CM, Howarth C, Mobbs P, Attwell D. 2006. Bidirectional control of CNS capillary diameter by pericytes. Nature. 443:700–704.
Pinard E, Engrand N, Seylaz J. 2000. Dynamic cerebral microcirculatory changes in transient forebrain ischemia in rats: involvement of type I nitric oxide synthase. J Cereb Blood Flow Metab. 20: 1648–1658.
Plouraboue F, Cloetens P, Fonta C, Steyer A, Lauwers F, Marc-Vergnes JP. 2004. X-ray high-resolution vascular network imaging. J Microsc. 215:139–148.
Reina-De La Torre F, Rodriguez-Baeza A, Sahuquillo-Barris J. 1998. Morphological characteristics and distribution pattern of the arterial vessels in human cerebral cortex: a scanning electron microscope study. Anat Rec. 251:87–96.
Riddle DR, Gutierrez G, Zheng D, White LE, Richards A, Purves D. 1993. Differential metabolic and electrical activity in the somatic sensory cortex of juvenile and adult rats. J Neurosci. 13:4193–4213.
Rodriguez-Baeza A, Reina-De La Torre F, Ortega-Sanchez M, Sahuquillo-Barris J. 1998. Perivascular structures in corrosion casts of the human central nervous system: a confocal laser and scanning electron microscope study. Anat Rec. 252:176–184.
Roy CS, Sherrington CS. 1890. On the regulation of the blood supply of the brain. J Physiol. 11:85–108.
Russ J, Dehoff R. 2000. Practical stereology. New York: Plenum Press.
Saleem KS, Logothetis NK. 2006. A combined MRI and histology Atlas of the Rhesus monkey brain. San Diego: Academic Press.
Sheth SA, Nemoto M, Guiou M, Walker M, Pouratian N, Hageman N, Toga AW. 2004. Columnar specificity of microvascular oxygenation and volume responses: implications for functional brain mapping. J Neurosci. 24:634–641.
Sheth SA, Nemoto M, Guiou M, Walker M, Pouratian N, Toga AW. 2004. Linear and nonlinear relationships between neuronal activity, oxygen metabolism, and hemodynamic responses. Neuron. 42:347–355.
Sheth SA, Nemoto M, Guiou MW, Walker MA, Toga AW. 2005. Spatiotemporal evolution of functional hemodynamic changes and their relationship to neuronal activity. J Cereb Blood Flow Metab. 25:830–841.
Stewart PA, Isaacs H, LaManna JC, Harik SI. 1997. Ultrastructural concomitants of hypoxia-induced angiogenesis. Acta Neuropathol (Berl). 93:579–584.
Thomsen K, Offenhauser N, Lauritzen M. 2004. Principal neuron spiking: neither necessary nor sufficient for cerebral blood flow in rat cerebellum. J Physiol. 560:181–189.
Tieman SB, Mollers S, Tieman DG, White J. 2004. The blood supply of the cat's visual cortex and its postnatal development. Brain Res. 998:100–112.

Turner R. 2002. How much cortex can a vein drain? Downstream dilution of activation-related cerebral blood oxygenation changes. Neuroimage. 16:1062–1067.
Vanzetta I, Slovin H, Omer DB, Grinvald A. 2004. Columnar resolution of blood volume and oximetry functional maps in the behaving monkey; implications for FMRI. Neuron. 42: 843–854.
Weber B, Burger C, Wyss MT, von Schulthess GK, Scheffold F, Buck A. 2004. Optical imaging of the spatiotemporal dynamics of cerebral blood flow and oxidative metabolism in the rat barrel cortex. Eur J Neurosci. 20:2664–2670.
Wong-Riley M. 1979. Changes in the visual system of monocularly sutured or enucleated cats demonstrable with cytochrome oxidase histochemistry. Brain Res. 171:11–28.
Wong-Riley MT. 1989. Cytochrome oxidase: an endogenous metabolic marker for neuronal activity. Trends Neurosci. 12:94–101.
Wong-Riley MT, Welt C. 1980. Histochemical changes in cytochrome oxidase of cortical barrels after vibrissal removal in neonatal and adult mice. Proc Natl Acad Sci USA. 77:2333–2337.
Woolsey TA, Rovainen CM, Cox SB, Henegar MH, Liang GE, Liu D, Moskalenko YE, Sui J, Wei L. 1996. Neuronal units linked to microvascular modules in cerebral cortex: response elements for imaging the brain. Cereb Cortex. 6:647–660.
Yacoub E, Duong TQ, Van De Moortele PF, Lindquist M, Adriany G, Kim SG, Ugurbil K, Hu X. 2003. Spin-echo fMRI in humans using high spatial resolutions and high magnetic fields. Magn Reson Med. 49:655–664.
Zheng D, LaMantia AS, Purves D. 1991. Specialized vascularization of the primate visual cortex. J Neurosci. 11:2622–2629.